Supplementary Information

Fluorido-Bridged Robust Metal-Organic Frameworks for Efficient C$_2$H$_2$/CO$_2$ Separation under Moist Condition

Yi-Ming Gu,[a,b,‡] You-You Yuan,[c,‡] Cai-Lin Chen,[d,‡] Sheng-Sheng Zhao,[a] Tian-Jun Sun,[a] Yu Han,[d] Xiao-Wei Liu,[d,*] Zhiping Lai,[d,*] and Shu-Dong Wang [a,*]

[a] Dalian National Laboratory for Clean Energy, Dalian Institute of Chemical Physics, Chinese Academy of Sciences, Dalian, 116023, China.

[b] University of Chinese Academy of Sciences, Beijing 100049, China.

[c] Core Laboratory, King Abdullah University of Science and Technology (KAUST), Thuwal, 23955-6900, Saudi Arabia.

[d] Advanced Membranes and Porous Materials Center, Division of Physical Sciences and Engineering, King Abdullah University of Science and Technology (KAUST), Thuwal, 23955-6900, Saudi Arabia.

[*] E-mail: xiaowei.liu@kaust.edu.sa

zhiping.lai@kaust.edu.sa

wangsd@dicp.ac.cn

[‡]These authors contributed equally

Supplementary Figures 1-21

Supplementary Tables 1-11

Reference

This supplementary material includes:

Section 1 Materials synthesis

Chemicals and Preparation of DNL-9(Fe): Ferric chloride hexahydrate ($FeCl_3 \cdot 6H_2O$, > 99%, AR, Sinopharm), 2,5-furandicarboxylic acid (abbr. FDCA, 99%, AR, Meryer), N, N-dimethylformamide (DMF, 99% AR, Aladdin), hydrofluoric acid (HF, >40 wt.% aq., Sinopharm), trifluoroacetic acid (abbr. TFA, >99.9% AR, Macklin) and alcohol (EtOH, >99.7%, AR, Aladdin) were all used as received unless otherwise stated. 0.144 g of $FeCl_3 \cdot 6H_2O$ (0.535 mmol) and 0.092 g of 2,5-furandicarboxylic acid (0.798 mmol) were added into a 20 ml Teflon liner containing 11 ml of DMF. After stirring for 10 min, 0.2 ml of TFA and 50 µl of HF (1.071 mmol) were quickly injected into the solvent under stirring (careful, white hazardous fog). The resultant mixture in the capped liner was then put in the ultrasound for 20 min. Next, the liner was sealed in a high-pressure stainless-steel autoclave, and heated in the oven at 423 K for 2 days (heating rate: 2 K/min). After naturally cooling down, the products were collected by filtration and thoroughly washed with DMF. To totally evacuate the guest molecules, the products could be soaked in DMF for 3 days and alcohol for another 2 days: the solvents all replenished once a day. The samples were then dried in a dynamic vacuum oven at 333 K overnight and obtained for future use (Yield >90%).
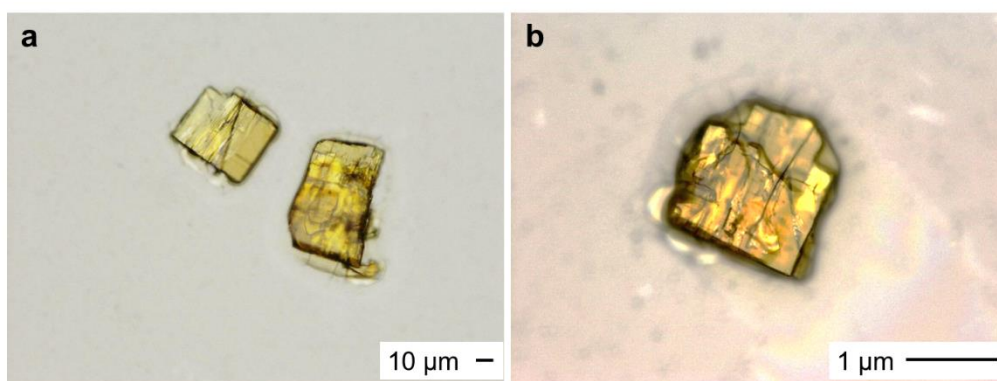

Fig. S1 Optical images of single crystals of DNL-9(Fe) at different magnifications

Mass spectrometry analysis: The qualitative analysis of the product gases, generated from the partial decomposition of DMF in the presence of TFA and a high temperature of 423 K during the synthesis, was conducted using the time-of-flight mass spectrometry (TOFMS) in the Key Laboratory of Separation Science for Analytical Chemistry, DICP, China. The TOF signals were recorded by a 100 ps time-to-digital converter (TDC) (model 9353, Ametec Inc., Oak Ridge, U.S.A.) with a repetition rate of 25 kHz, while all the mass spectra were accumulated for 60 s. A mass resolution of 6000 (fwhm) was achieved at m/z 78 with a 450 mm long field-free region.[1, 2] Additionally, the TOF signals of O_2 and N_2 are detected due to the blank from the instrument.
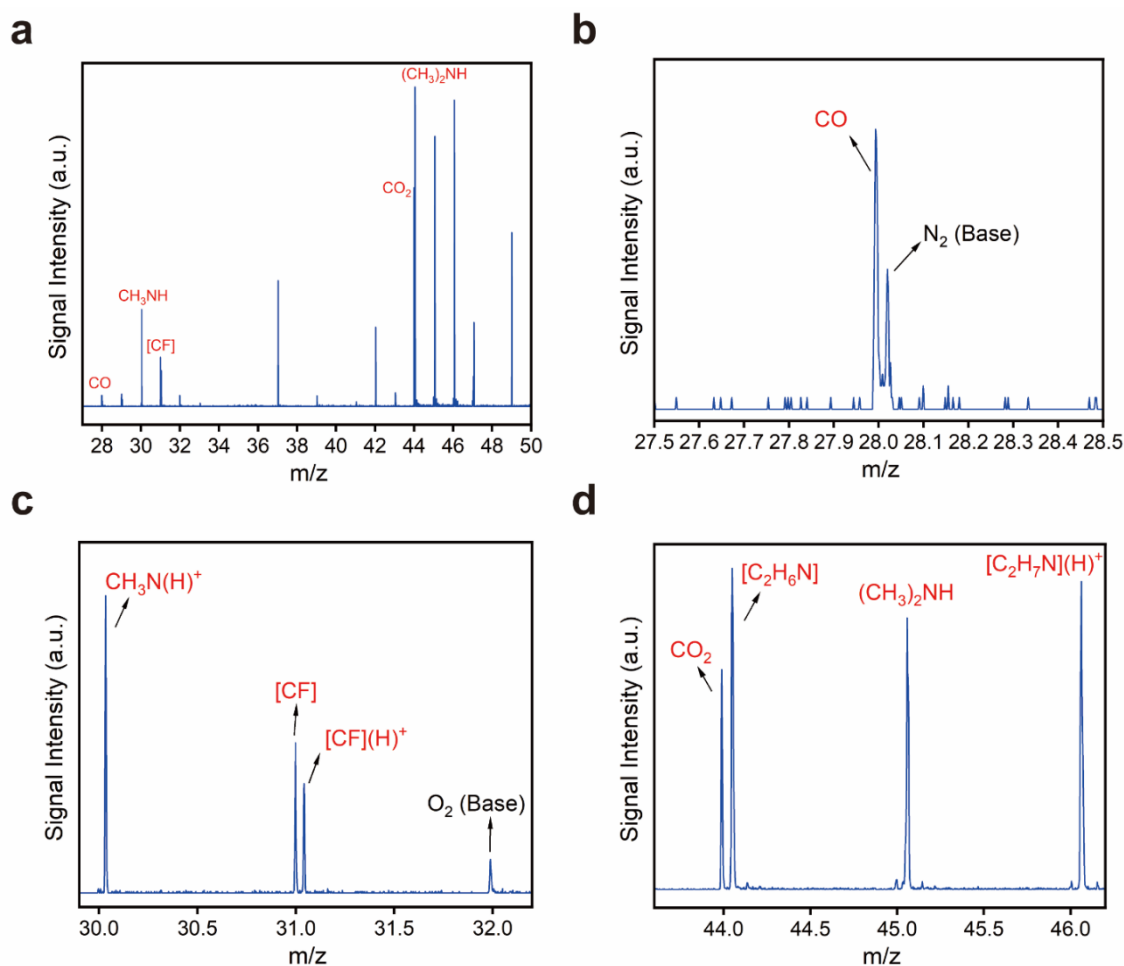

Fig. S2 The qualitative mass TOFMS spectrum of reaction products. Zoom in the spectrum of **(a)** 27-50 m/z; **(b)** 27.5-28.5 m/z; **(c)** 30.0-32.0 m/z and **(d)** 43.0-46.4 m/z

Section 2 Materials characterization

Crystal structure determination and refinement by single-crystal diffraction: The single-crystal XRD data for DNL-9(Fe) were collected on a Bruker D8 Venture CMOS-based diffractometer (Mo-Kα radiation, λ = 0.71073 Å) using the SMART and SAINT programs. The parameters of final unit cell were based on all observed reflections from integration of all frame data. The structures were solved in the space group by direct method and refined by the full-matrix least-squares method fitting on F^2.[3] For all compounds, all non-hydrogen atoms were refined anisotropically. The hydrogen atoms of organic ligands were located geometrically and fixed isotropic thermal parameters. The structures were determined by SHELXT and refined with a two-component twinned crystal using the Olex2 software package.[4] The disordered non-coordinated solvents were all removed using the PLATON SQUEEZE program.[5-8] Refinement results are summarized in **Table S1**. Crystallographic data in CIF format have been deposited in the Cambridge Crystallographic Data Centre (CCDC) under CSD Entry 2050430. The data can be obtained free of charge via www.ccdc.cam.ac.uk/data_request/cif (or from the Cambridge Crystallographic Data Centre, 12 Union Road, Cambridge CB2 1EZ, U.K.).

Table S1. Crystallographic data and refinement for DNL-9(Fe)

Identification code	DNL-9(Fe)
Formula weight	1493.96
Empirical formula	$C_{24}H_8F_{14}Fe_6O_{20}$ +6(C_2H_8N) (solvent)
Temperature (K)	110
Volume (Å^3)	6359.3(7)
Wavelength (Å)	MoKα ($\lambda = 0.71073$)
Crystal system	Orthorhombic
Space group	$P\ 2_12_12_1$
a (Å)	16.8365(11)
b (Å)	18.0784(13)
c (Å)	20.740(12)
d_{calc} (g/cm^3)	1.565
Z	4
μ (mm^{-1})	1.449
F(000)	3000
2θ range for data collection	4.612 to 55.048
Refinement method	Full-matrix least-squares on F^2
Goodness-of-fit on F^2	1.034
Index ranges	-21<h<21, -23<k<23, -26<l<26
Completeness	0.99
Reflections collected	43177
Independent reflections (R_{int})	14488 [Rint = 0.0858, Rsigma = 0.1094]
Final R indices [I>2σ(I)]	R1 = 0.0668 , wR2 = 0.1487
R indices (all data)	R1 = 0.1092 , wR2 = 0.1689
Largest diff. peak and hole (e/Å^3)	0.95/-0.94
Twin law	-1 0 0 0 -1 0 0 0 -1
Twin Ratio	0.48(3)/0.52

Elemental analysis: The chemical composition of DNL-9(Fe) was jointly determined by X-ray fluorescence (XRF) measurement and nonmetallic elemental analysis: Compositions of Fe and F were obtained via XRF measurement on Zetium; Compositions of O, N and H were tested via elemental analysis on Horiba, EMGA-930 at 3773 K (3500℃) with He flow, whilst C and S were determined via elemental analysis on Horiba, EMIA-8100 at 1723 K (1450℃) with O_2 flow. Before test, the sample was heating at 433 K under vacuum for removing guest molecules.

Table S2. Chemical composition determined by XRF (FeF) and elemental analysis (CS, ONH) for guest-free DNL-9(Fe)

XRF data	Gravimetric concentration %	Atomic concentration %
Fe %	31.42	9.5
F %	18.86	16.8
CS elemental analysis	Gravimetric concentration %	Atomic concentration %
C %	24.15	34.1
S %	0	0
ONH elemental analysis	Gravimetric concentration %	Atomic concentration %
O %	25.43	26.9
N %	0.07	0.1
H %	0.75	12.6
Exp. empirical formula	$C_{24}H_{8.45}F_{12.10}Fe_{6.86}O_{19.07}+(C_2H_8N)_{0.06}$	

Mössbauer spectra analysis: The mössbauer spectra of DNL-9(Fe) were recorded on a conventional spectrometer with alternating constant acceleration of the γ-source (^{57}Co/Rh, 1.85 GBq), which was kept at room temperature. The minimum experimental line width was 0.24 mm/s (full width at half-height). Isomer shifts are quoted relative to alpha iron metal at 298 K. The ground state: I_g = 1/2, E_g = 0 keV, g_g = 0.1808, μ_g = 0.0904 μ_N, Q_g = 0 barn; The excited state: I_e = 3/2, E_e = 14.4129 keV, g_e = -0.1032, μ_e = -0.1549 μ_N, Q_g = 0.16 barn.

Table S3. Mössbauer fitting parameters of DNL-9(Fe) recorded at 298 K

Assignment	Area [%]	δ	ΔE_Q	Γ
Fe^{2+}	33.31%	1.2528	2.9929	0.2448
Fe^{3+}	66.69%	0.4454	0.6121	0.2628

δ = Centroid shift (mm/s);

ΔE_Q = Quadrupole splitting (mm/s);

Γ = Full width at half maximum (mm/s).

Solid state ^{19}F Magic Angle Spinning Nuclear Magnetic Resonance analyses (^{19}F-MAS NMR): Solid-state ^{19}F MAS NMR experiments were performed on a Bruker Avance III 400 spectrometer equipped with a 9.4 T wide-bore magnet using a 4 mm MAS probe and 12000 rps. The chemical shifts were referenced to $C_2H_4O_2F_3N$ with peak at 76.8 ppm. The weak signal of F is possibly due to the paramagnetic shielding effect of Fe. The asterisks feature the sidebands of the characteristic peaks of Fe-F and Fe-F-Fe in NMR.
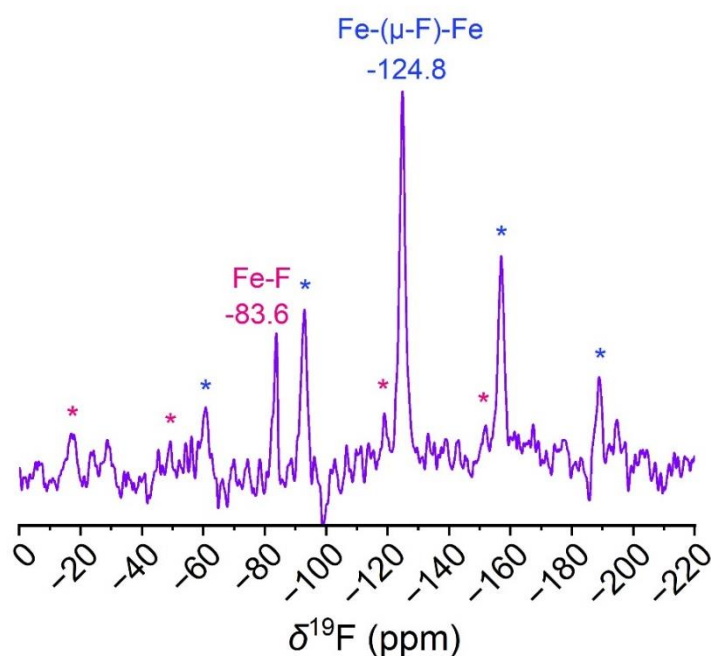

Fig. S3 ^{19}F MAS-NMR spectrum of DNL-9(Fe)

Powder X-ray diffraction: The Powder X-ray Diffraction (PXRD) patterns of different DNL-9(Fe) samples were measured on a PANalytical X'Pert Powder X-ray powder diffractometer with a voltage of 40 kV and a current of 40 mA (Cu Kα radiation, λ = 1.5406 Å). Due to the lattice orientation in the layered structure of the sample, the data were collected under transmission-mode powder diffraction in capillaries.
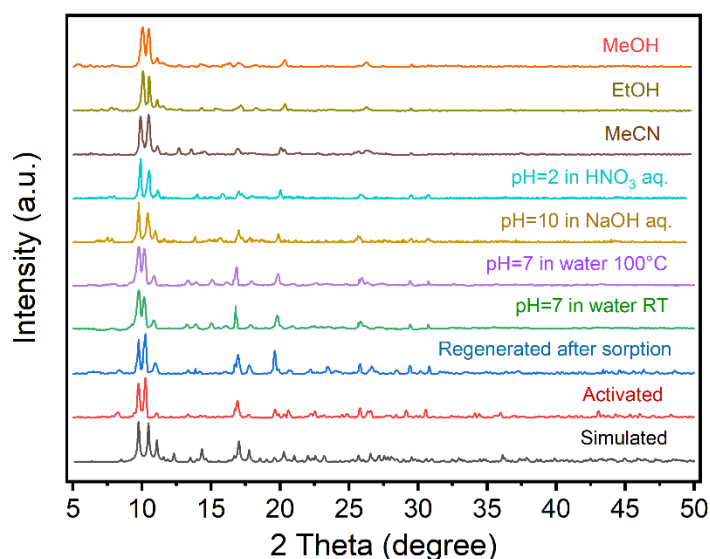

Fig. S4 PXRD patterns of different DNL-9(Fe) samples under transmission-mode powder diffraction in capillaries. From bottom to top: the simulated guest-free structure (CSD Entry 2050430: first remove all guest molecules, then structure optimized with cell fixed), the activated sample, the activated sample after five adsorption cycles under moist conditions in breakthrough tests, the activated sample after exposure to 25 °C and 100 °C water, NaOH solution (pH=10), HNO₃ solution (pH=2), MeCN, EtOH and MeOH for 24 h

Porosity and thermogravimetric analysis: The porosity was calculated from the argon sorption isotherms performed at 87 K in liquid argon. The linearity of fitting for the Brunauer-Emmett-Teller (BET) area were calculated via applying the Rouquerol consistency;[9] total pore volume (V_p) was obtained at P/P_0=0.90; micropore volume (V_{mic}) was computed by t-Plot method;[10] pore size distributions (PSD) were calculated

using the NLDFT Ar (87 K) and N_2 (77 K) zeolite kernel with a cylindrical pore model. Thermogravimetric analysis (TG) and differential scanning calorimetry (DSC), as well as mass spectra (MS) were all collected on a simultaneous thermal-mass spectrometer analyzer (TG-MS), i.e., NETZSCH STA 449F5 and Pfeiffer Vacuum GSD350 Thermo Star. The samples were heated from 313 K to 1073 K with a heating rate of 10 K/min in a dynamic air atmosphere.
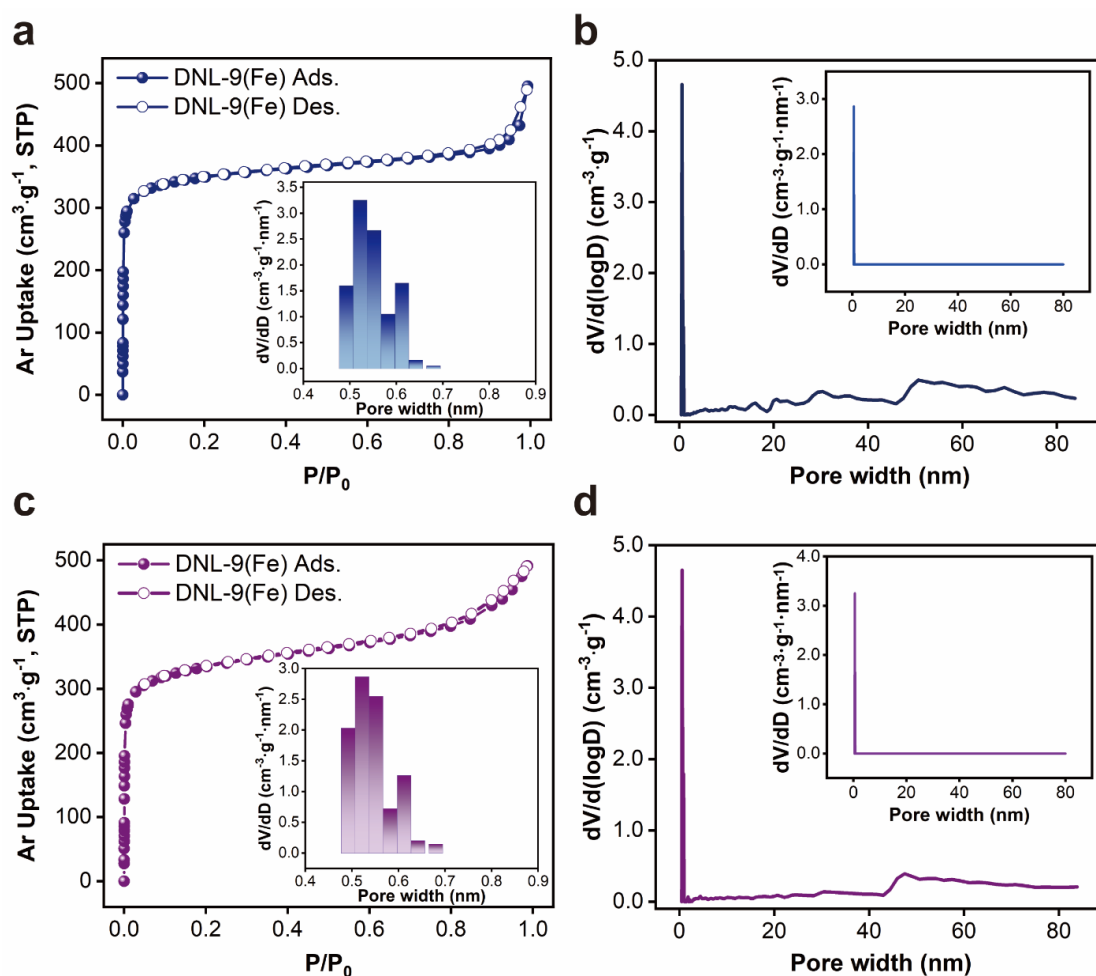

Fig. S5 Argon adsorption/desorption (solid/open) isotherms at 87 K and DFT-pore size distribution. **(a-b)** as-synthesized DNL-9(Fe); **(c-d)** regenerated DNL-9(Fe) after adsorption
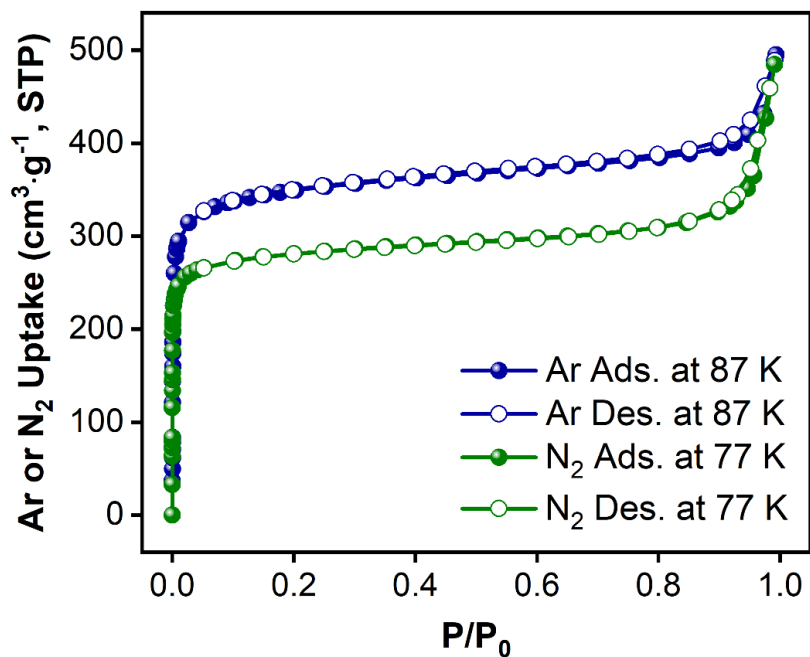
Fig. S6 The comparison of Ar (at 87 K) and N_2 (at 77 K) adsorption/desorption (solid /open) isotherms of DNL-9(Fe)

Table S4. The textural properties of DNL-9(Fe)

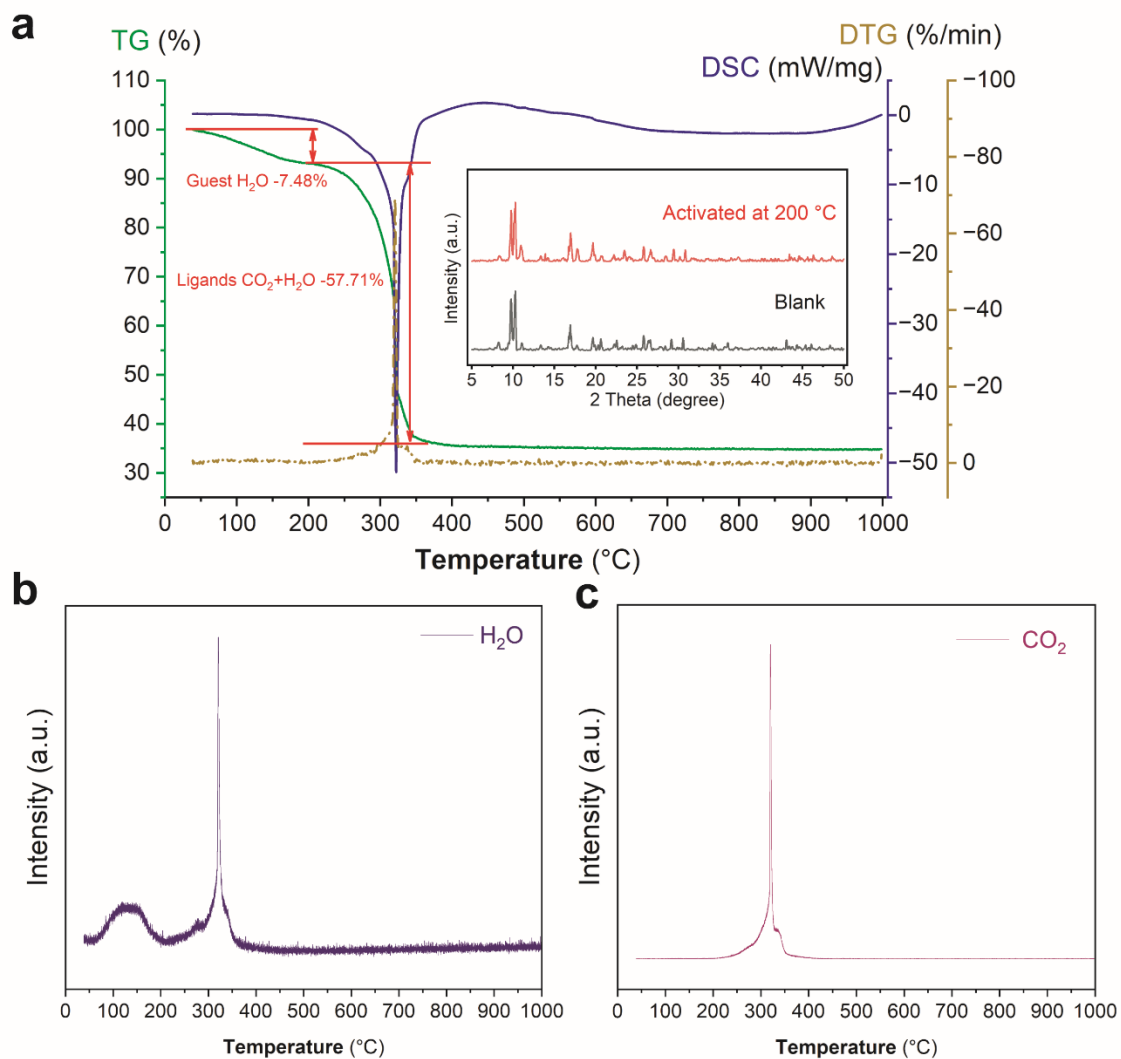| Adsorbate	Ar @ 87 K		N_2 @ 77 K
Adsorbent	Fresh	Regenerated	Fresh
BET area, m^2/g	1135	1131	1113
Average pore size, Å	5.5	5.5	5.8
Pore volume, V_p, cm^3/g	0.50	0.49	0.50
Micropore volume, V_{mic}, cm^3/g	0.38	0.38	0.41

S10

Fig. S7 (a) TG, DSC and DTG curves of DNL-9(Fe) sample under air atmosphere. Inset: XRD patterns of fresh and activated samples (at 200 °C) of DNL-9(Fe). The qualitative mass spectra of **(b)** H_2O and **(c)** CO_2 releasing signal intensity collected on the TG-MS equipment.

Low-dose motion-corrected high-resolution TEM (HRTEM) and scanning electron microscope (SEM): HR-TEM imaging was performed on a Cs-corrected FEI G2 cubed Titan 60-300 electron microscope equipped with a Gatan K2 Summit direct-detection electron-counting camera operated under 300 kV. SEM images were taken on a JSM-7800F instrument (JEOL Company) with an acceleration voltage of 3 kV.
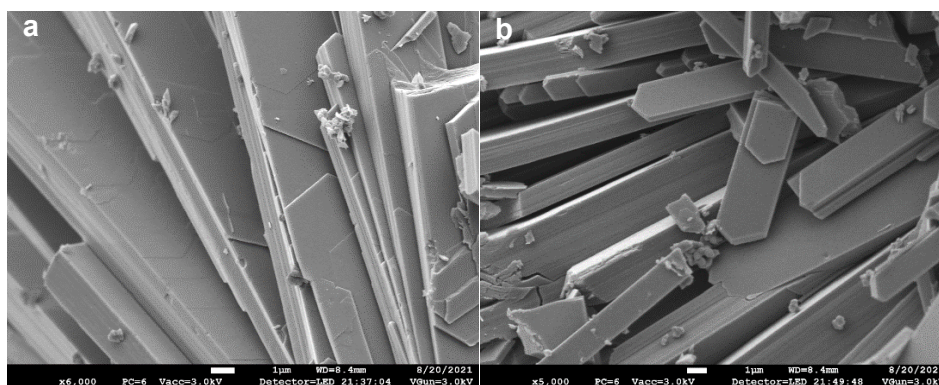
Fig. S8 SEM images of DNL-9(Fe) powder samples

Fourier transform infrared (FTIR) and Raman spectroscopy: FT-IR spectra was recorded in solid state using a Nicolet 6700 FT-IR instrument equipped with a KBr beam splitter and an MTC nitrogen-cooled detector. Before experiments, MOF samples and KBr powder were heating under an infrared lamp for 4 h. The spectra data were collected with the frequency of 4000-500 cm^{-1} at a resolution of 4 cm^{-1}. Raman spectra of blank and gas-loaded samples were collected with a $\lambda = 514$ nm laser.

Section 3 Adsorption measurement and fitting details

Gas adsorption: Static adsorption isotherms of C_2H_2 and CO_2 were measured on a Quantachrome Autosorb-iQ2 instrument at 288, 298 and 308 K (water bath) and 87 K (liquid argon bath). The gases were commercial with an ultra-high purity of 99.9% for C_2H_2, and 99.999% for CO_2 and Ar. Prior to adsorption, DNL-9(Fe) samples were first evacuated under a dynamic vacuum in Autosorb-iQ2 at 353 K for 4 h, and then activated to 433 K at the rate of 3 K/min for 18 h.
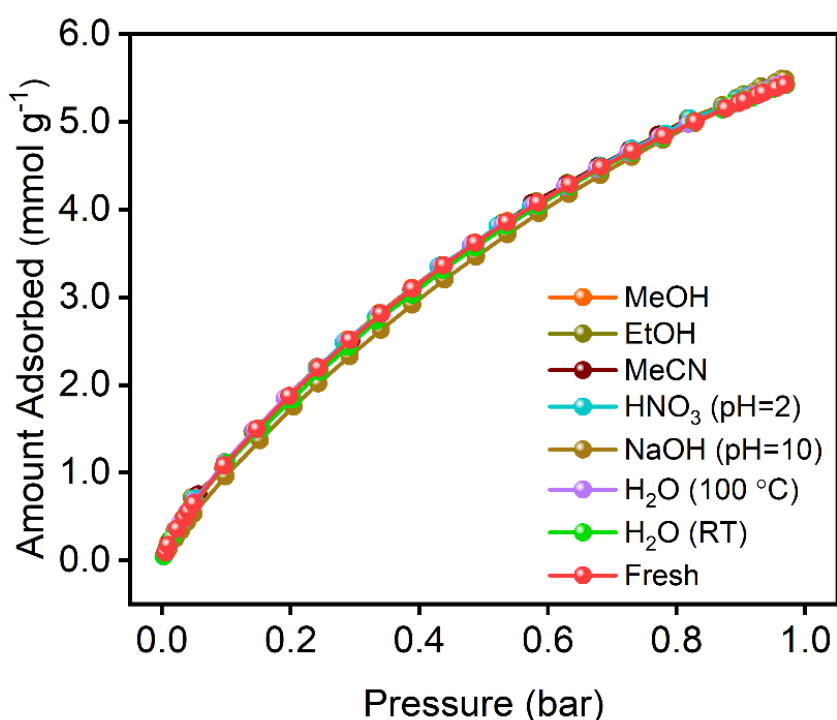
Fig. S9 C_2H_2 adsorption isotherms at 298 K for various DNL-9(Fe) samples after immersion in different solutions or solvents for 24 h

Water microcalorimetric and adsorption measurement: Water microcalorimetric measurement was performed on a BT2.15 heat-flux calorimeter, which was connected to a gas handling and a volumetric system employing MKS Baratron Capacitance Manometers for precise determination of pressure. The microcalorimetric system was operated under an ultimate dynamic vacuum of 10^{-7} Torr. Fresh samples were first heated at 433 K under vacuum overnight in a special glass cell, and then the cell was placed into the high vacuum system and stabilized for 12 h. The microcalorimetric data

was collected through sequentially introducing small doses (0.2 torr) of water vapor into the system under 313 K, with the relative pressure of injection increased gradually (~10 torr). Water adsorption isotherms could then be obtained, and the differential adsorption heat versus adsorbate coverage was tabulated. Water sorption isotherm of DNL-9(Fe) was measured on an IGA-100 instrument (Hiden Isochema Ltd.). Prior to adsorption, powder sample was fully regenerated at 433 K under a dynamic vacuum.
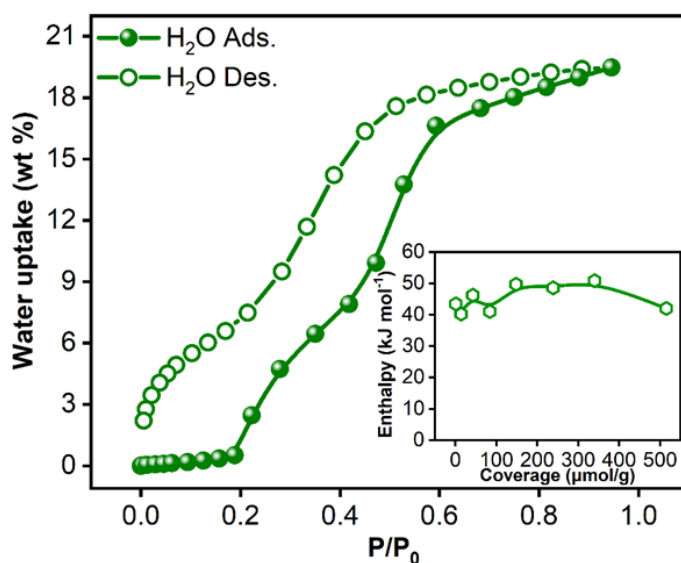

Fig. S10 The water sorption isotherm and enthalpy (insert) at 298 K

Table S5. Differential adsorption heat of H_2O on DNL-9(Fe)

Sorbent	H_2O initial loading		H_2O final loading	
	Heat (kJ/mol)	Coverage (mmol/kg)	Heat (kJ/mol)	Coverage (mmol/kg)
DNL-9(Fe)	43.49	1.23	42.01	515.63

Breakthrough experiments: As shown in **Fig. S11**, dynamic adsorption experiments via breakthrough tests were carried out using a homemade setup.[11] The adsorption fixed bed was a 250 mm length and 4 mm inner-diameter tube, packed with ca. 1.35 g of activated DNL-9(Fe) (particle size: 0.20~0.28 mm). Samples were completely activated under a He flow at 433 K overnight, and then cooled down to room temperature using a temperature-programmed water bath. Breakthrough experiments were performed with flow rates of 5 ml/min for C_2H_2/CO_2 mixtures (50/50, v/v) under dry and wet (ca. 90% RH) conditions, which were adjusted by a vapor generator. For wet conditions, the adsorbent column was pre-humidified before tests (**Fig. S12**). The composition of the gas from outlet was online detected by a mass spectrometry. All breakthrough experiments in this work were operated under constant conditions.
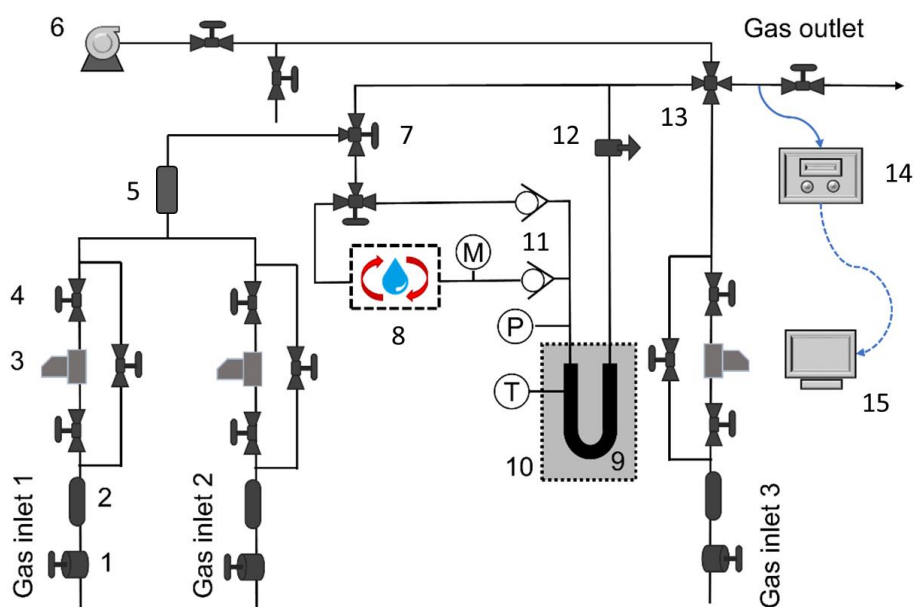
Fig. S11 Schematic setup for breakthrough experiments[11]

1 pressure reducing regulator; 2 gas purifier; 3 mass flow controller; 4 two-way valve; 5 vapor filter; 6 vacuum pump; 7 three-way valve; 8 vapor generator; 9 adsorbent bed; 10 thermostatic chamber; 11 one-way valve; 12 back pressure regulator; 13 four-way connection; 14 mass spectrometer; 15 computer
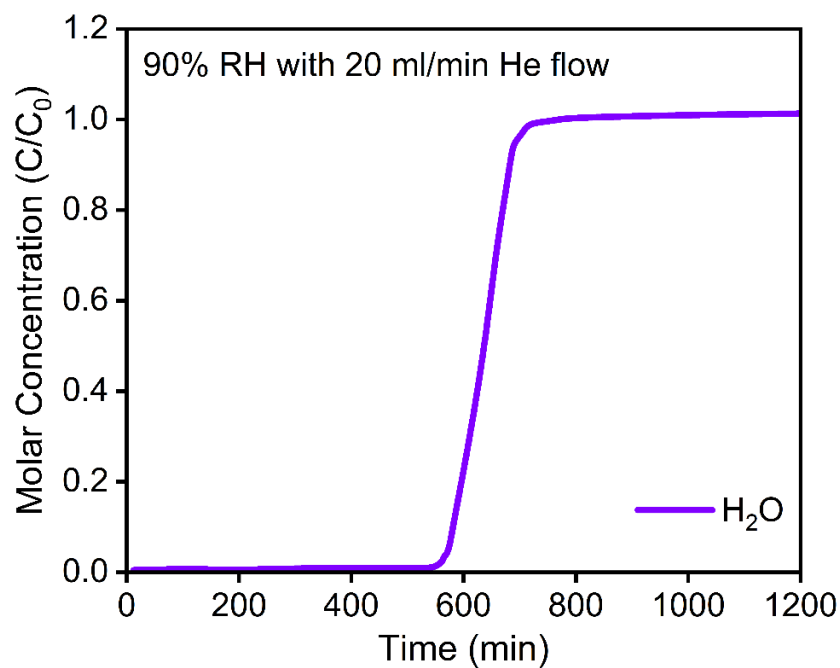
Fig. S12 Water breakthrough curve in a wet He stream (90% RH, 20 ml/min) at 298 K and 1 bar

Fig. S13 The experimental breakthrough curves for binary C_2H_2/CO_2 mixtures (50/50, v/v) on DNL-9(Fe) under wet (ca. 90% RH) conditions at 298, 308 and 318 K and 1 bar.

Fitting details for the adsorption isotherms: The C_2H_2 and CO_2 gas adsorption isotherms were all fitted using the following Dual-Site Langmuir-Freundlich (DSLF) model:

$$q = q_1 \frac{b_1 p^{c_1}}{1+b_1 p^{c_1}} + q_2 \frac{b_2 p^{c_2}}{1+b_2 p^{c_2}} \qquad (1)$$

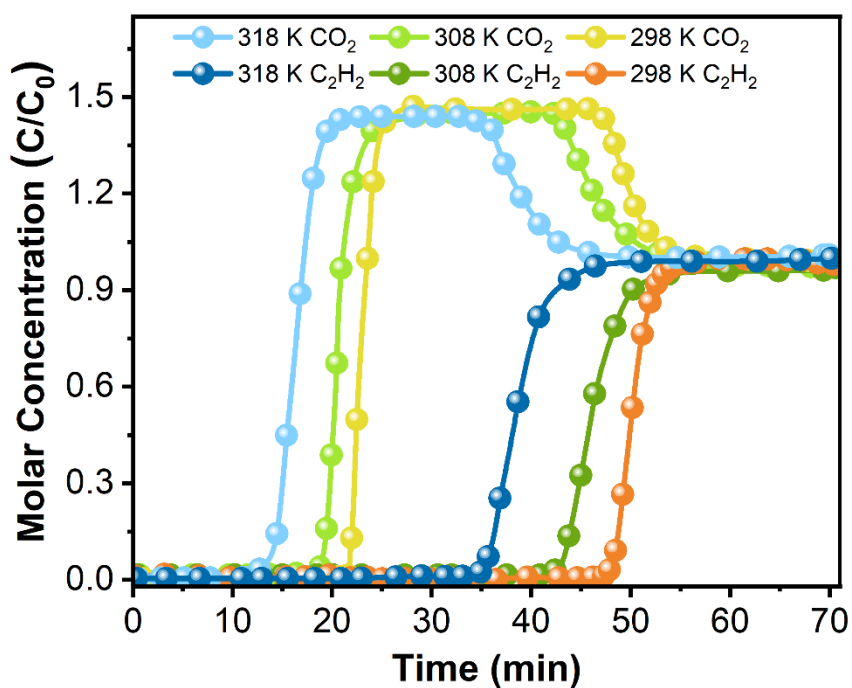Where q_1 and q_2 is the pure gas saturated capacities (mmol·g^{-1}) of site 1 and site 2 at different pressure (kPa); q is the equilibrium adsorbed amount of C_2H_2 or CO_2 in DNL-9(Fe) (mmol·g^{-1}); b_1 and b_2 are the affinity coefficients of site 1 and site 2 (kPa^{-1}); c_1 and c_2 suggest the system heterogeneity of the two sites.[12]

Calculation of adsorption enthalpy: Experimental isosteric enthalpy of adsorption (Q_{st}) of C_2H_2 and CO_2 were obtained using the Clausius-Clapeyron equation based on the adsorption data collected at 288, 298 and 308 K:[13]

$$\left(\frac{Q_{st}}{R}\right) = \left(\frac{\partial \ln P}{\partial \left(\frac{1}{T}\right)}\right)_\theta \qquad (2)$$

Where T is the temperature, P is the pressure, R is the ideal gas constant and θ indicates a certain and constant coverage status.

Calculation of static and dynamic selectivities: We used the ideal adsorbed solution theory (IAST) to predict the separation performance of gas mixtures on MOF adsorbents simply based on the pure component adsorption isotherms.[14] The adsorption isotherms were first fitted using the DSLF model as formula of (1).

The static C_2H_2/CO_2 IAST selectivities were then calculated as:

$$S_{i,j} = \frac{(n/y)_i}{(n/y)_j} \qquad (3)$$

Where i and j represent the two different gases, y is the proposed mole fraction of the corresponding gas in the mixture.

The dynamic adsorption selectivity of C_2H_2/CO_2 were computed based on the breakthrough curves. The selectivity was calculated via the formula of (3) and (4):[15]

$$q_i = \frac{\left(F_{0,i}C_{0,i}t_1 - \int_0^{t_1} F_i C(t)dt\right) - V_d}{m} \qquad (4)$$

q_i is the adsorption capacity of C_2H_2 or CO_2 (mmol·g⁻¹); F_i is the flow rate of the component i in binary mixture gases; $C(t)$ is the concentration of the component i in the gas phase at instantaneous t; t_1 is the stable moment when the component i leaving the column in the breakthrough experiments, and V_d is the dead volume of the mixed bed setup; m is the weight of DNL-9(Fe) used.
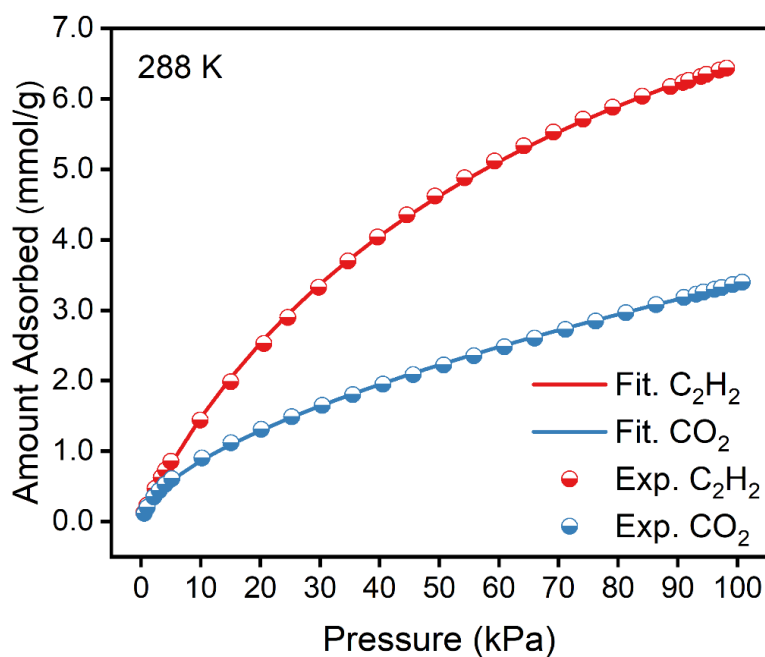
Fig. S14 Experimental and DSLF fitting adsorption isotherms of C_2H_2 and CO_2 on DNL-9(Fe) at 288 K
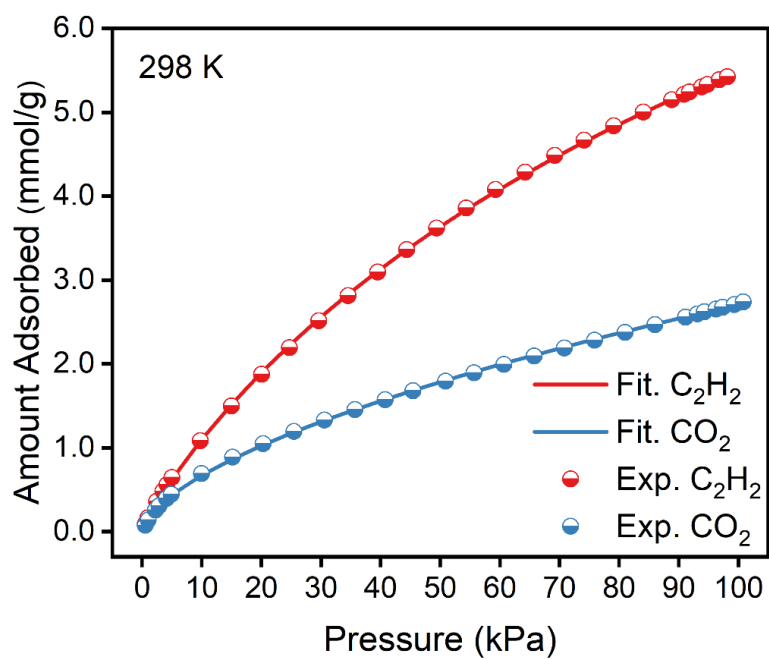
Fig. S15 Experimental and DSLF fitting adsorption isotherms of C_2H_2 and CO_2 on DNL-9(Fe) at 298 K
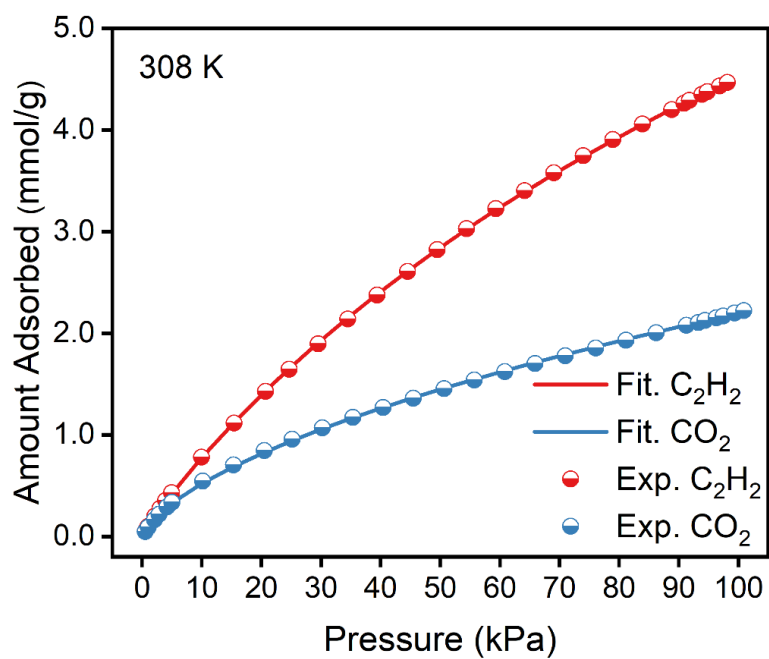
Fig. S16 Experimental and DSLF fitting adsorption isotherms of C_2H_2 and CO_2 on DNL-9(Fe) at 308 K
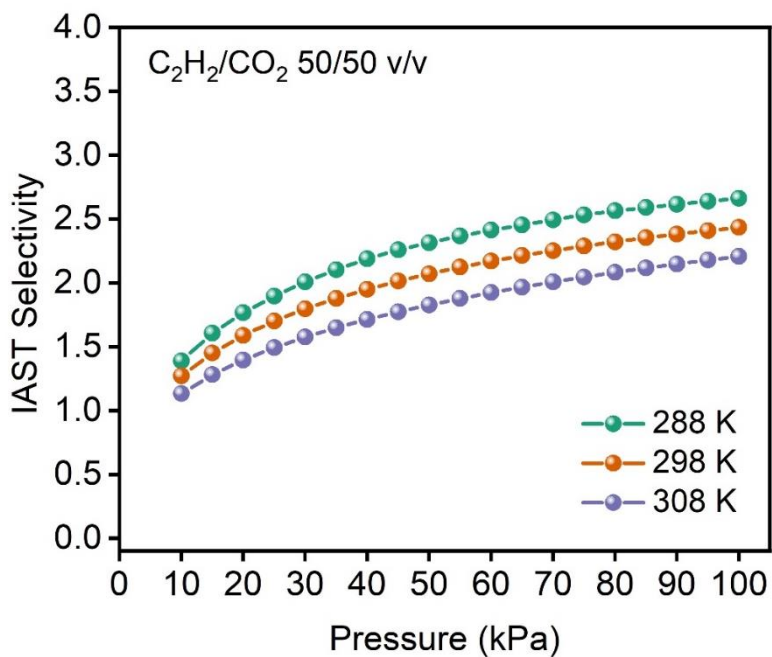
Fig. S17 IAST selectivities for equimolar C_2H_2/CO_2 mixtures at different pressure and temperature

Table S6. The DSLF fitting parameters for C_2H_2 and CO_2 adsorption at different temperatures

Temperature (K)	288		298		308	
Gas	C_2H_2	CO_2	C_2H_2	CO_2	C_2H_2	CO_2
q_1	11.6938	4.3322	10.0169	4.0516	9.4750	3.9006
b_1	0.0165	0.0161	0.0191	0.0280	0.0173	0.0262
c_1	0.9388	0.5631	0.8791	0.6103	0.9186	0.6682
q_2	0.7381	1.2609	0.8065	1.0351	1.0281	0.9424
b_2	0.0009	0.0009	0.0026	0.0008	0.0011	0.0008
c_2	0.5143	1.2852	0.5549	1.0378	0.5246	0.7103
R^2	0.9999	0.9969	0.9999	0.9999	0.9999	0.9987

Table S7 The dynamic adsorption capacity and selectivity from breakthrough curves at 298 K and 1 bar

	q_{C2H2} (mol/kg)	q_{CO2} (mol/kg)	Selectivity
5 ml/min dry mixture gas	3.91	1.58	2.48
5 ml/min wet mixture gas	3.83	1.52	2.52

Kinetic analysis: The following equation (5) is utilized to correlate the gas diffusion coefficients in DNL-9(Fe) with experimental adsorption data [16, 17]. The kinetic adsorption curves were collected on IGA-100 instrument (Hiden Isochema Ltd.) at 298 K. Prior to the adsorption measurement, sample with uniform particles (0.20~0.28 mm) was fully regenerated at 433 K under a dynamic vacuum:

$$\frac{M_t}{M_\infty} = 1 - \frac{6}{\pi^2} \sum_{n=1}^{\infty} \frac{1}{n^2} e^{\left(-\frac{Dn^2\pi^2 t}{r^2}\right)} \quad (5)$$

M_t is the adsorption uptake of C_2H_2 or CO_2 in the moment of t (mol·g^{-1}); M_∞ is the adsorption capacity in a state of equilibrium (mol·g^{-1}); r is the radius of spherical-sharped DNL-9(Fe) (0.09~0.12 mm); D is the diffusion coefficient (m^2·s^{-1}).

When $M_t/M_\infty > 70\%$, n≈1. The formula of (5) could be simplified as following:

$$\frac{M_t}{M_\infty} = 1 - \frac{6}{\pi^2} e^{\left(-\frac{D\pi^2 t}{r^2}\right)} \quad (6)$$

Table S8 Diffusion coefficients of C_2H_2 and CO_2 on DNL-9(Fe) at 5 mbar and 298 K

Adsorbate	Diffusion Coefficient (m^2·s^{-1})	$D \cdot r^{-2}$ / s^{-1}
C_2H_2	4.40×10^{-12}	5.43×10^{-4}
CO_2	8.63×10^{-12}	1.07×10^{-3}
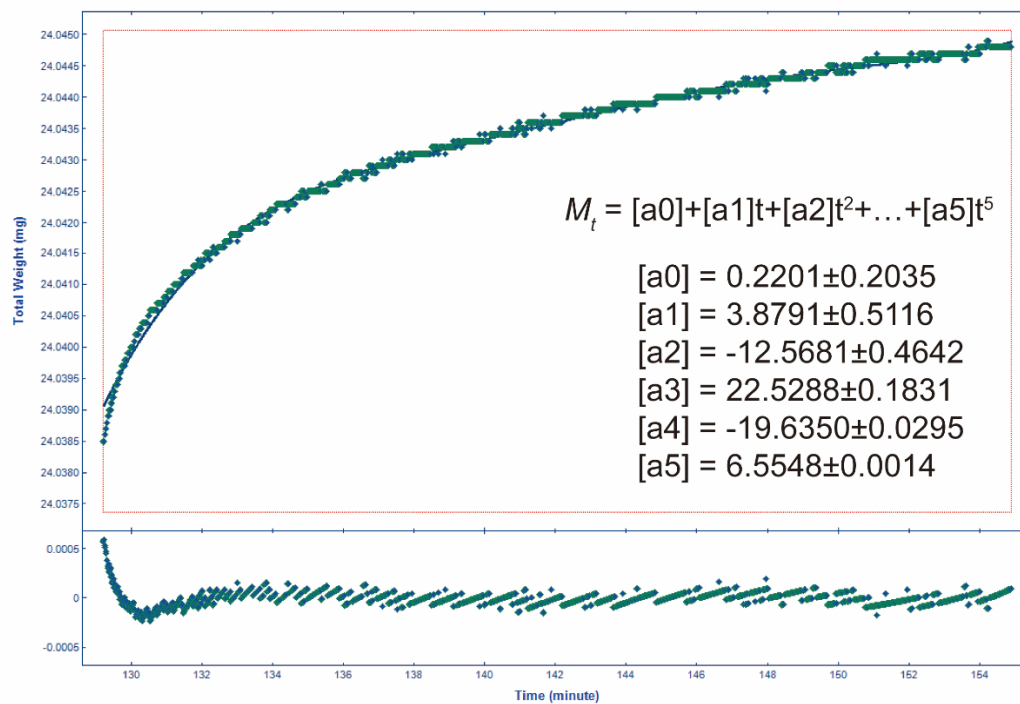
Fig. S18 The kinetic adsorption curve of C_2H_2 on DNL-9(Fe) at 5 mbar

$$M_t = [a0]+[a1]t+[a2]t^2+\ldots+[a5]t^5$$

$[a0] = 0.2201\pm0.2035$
$[a1] = 3.8791\pm0.5116$
$[a2] = -12.5681\pm0.4642$
$[a3] = 22.5288\pm0.1831$
$[a4] = -19.6350\pm0.0295$
$[a5] = 6.5548\pm0.0014$
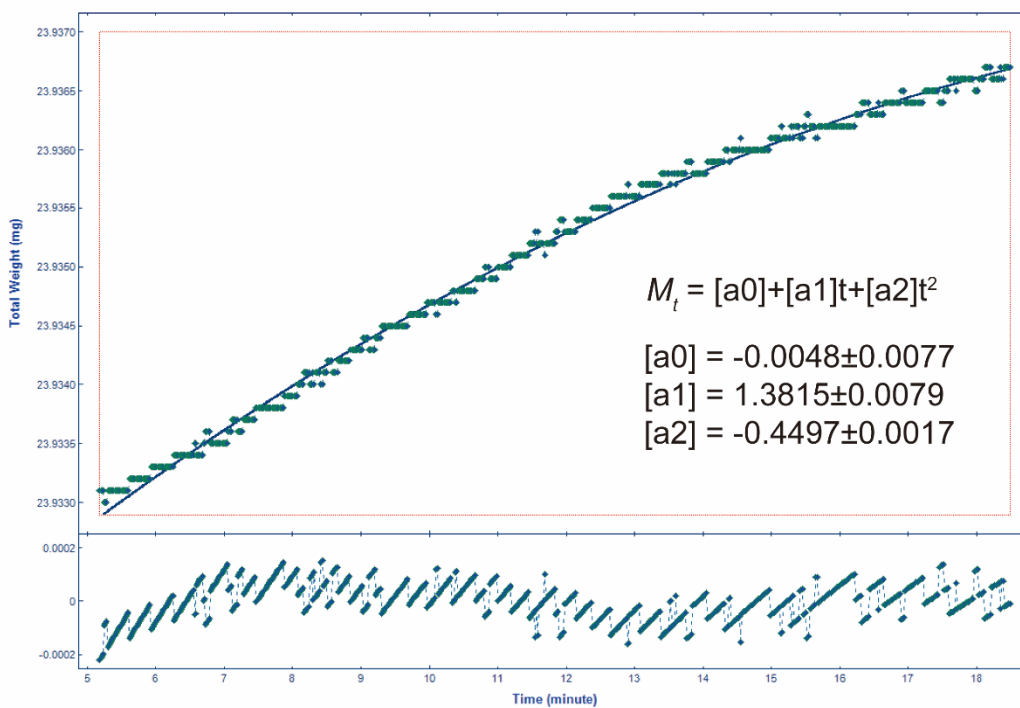
Fig. S19 The kinetic adsorption curve of C_2H_2 on DNL-9(Fe) at 5 mbar

$$M_t = [a0]+[a1]t+[a2]t^2$$

$[a0] = -0.0048\pm0.0077$
$[a1] = 1.3815\pm0.0079$
$[a2] = -0.4497\pm0.0017$

S22

Section 4 Molecular simulation

Density functional theory (DFT)-D3 calculations: First-principle calculations were performed by the DFT implemented in the Vienna Ab-initio Simulation Package (VASP) package, which were used to calculate the static binding energy, adsorption binding sites of C_2H_2, CO_2 and H_2O adsorbents, and the surface electrostatic potential of the framework.[18] The generalized gradient approximation (GGA) with the Perdew−Burke−Ernzerhof (PBE) functional were utilized to describe the electronic exchange and correlation effects. Uniform G-centered k-points meshes with a resolution of $2\pi*0.04$ Å^{-1} and Methfessel-Paxton electronic smearing were adopted for the integration in the Brillouin zone for geometric optimization.[19-21] The simulation was run with a cutoff energy of 500 eV throughout the computations. These settings ensured the convergence of the total energy within 1 meV per atom. Structure relaxation proceeded until all forces on atoms were less than 1 meV Å^{-1} and the total stress tensor was within 0.01 GPa of the target value.

The calculation of electrostatic potentials on the ground-state potential energy surfaces of MOFs have been performed by the DFT approach with the 6-31G basis set.[22] The Becke's three-parameter hybrid exchange functional and the Lee-Yang-Parr correlation functional (B3LYP) implemented in the GAUSSIAN 03 package have been used in the DFT calculation.[23, 24]

Static binding energies (ΔE) at 0 K were calculated using the following expression, where E refers to the total energy of the MOF+gas complex, the MOF, and gas molecule, respectively:

$$\Delta E = E_{\text{MOF+gas}} - E_{\text{MOF}} - E_{\text{gas}} \quad (7)$$
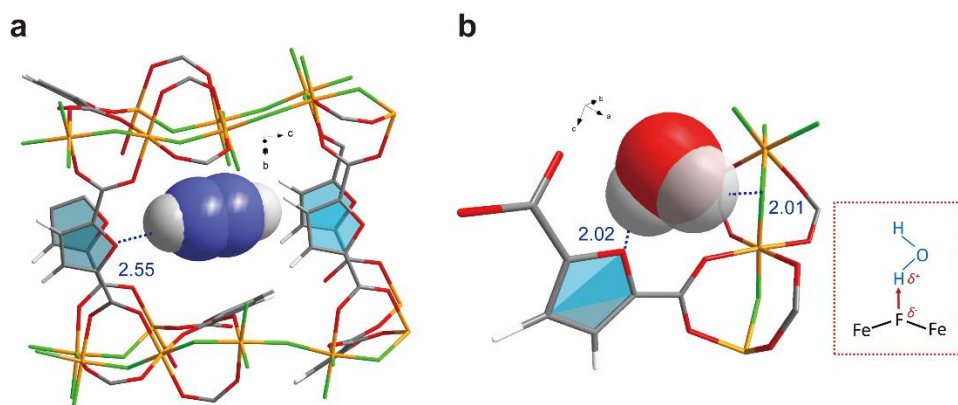
Fig. S20 The adsorption status of **(a)** C_2H_2 (site 2); **(b)** H_2O molecules in DNL-9(Fe) via DFT-D3 optimization
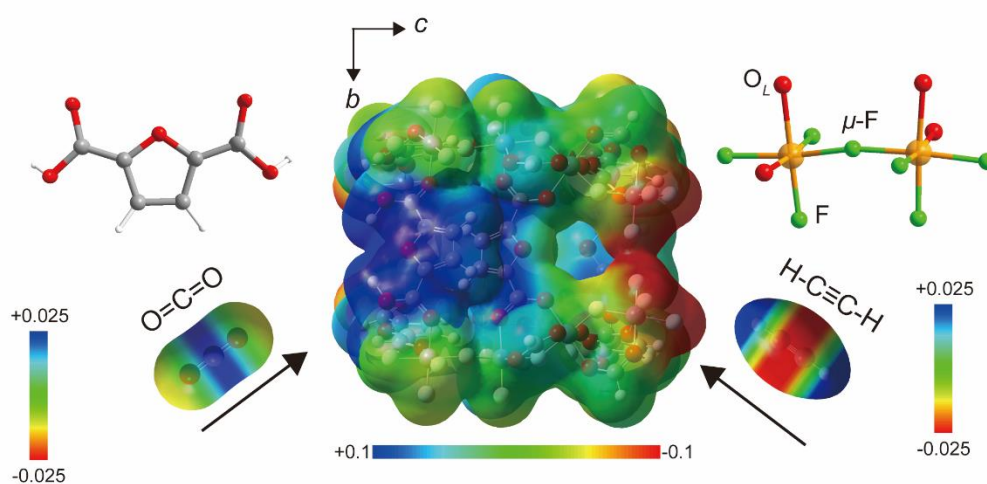
Fig. S21 Electrostatic potentials of C_2H_2, CO_2 and the framework. The scale bar: kcal mol^{-1}

Table S9 Static binding energies of C_2H_2, CO_2 and H_2O on DNL-9(Fe)

Molecule	$E_{(MOF+gas)}$	$E_{(MOF)}$	$E_{(gas)}$	$\Delta E_{(eV)}$	$\Delta E_{(kJ/mol)}$
CO_2	-1963.68	-1940.44	-22.95	-0.30	-28.56
C_2H_2 (Site 1)	-1963.71	-1940.44	-22.94	-0.33	-31.78
C_2H_2 (Site 2)	-1963.70	-1940.44	-22.94	-0.32	-30.64
H_2O	−1964.68	-1940.44	−14.23	−0.49	−47.46

Section 5 Summary

Table S10. The surface area, framework density, adsorption enthalpy, C_2H_2 capacity and C_2H_2/CO_2 IAST selectivity of the reported HBA-containing MOFs at 298 K and 1 bar

MOFs	BET *SA* (m²/g)	Density$^\square$ (g/cm³)	C_2H_2 capacity 298 K (mol/kg)	IAST selectivity 298K 50v/50v	$Q_{st}^\dagger$ (kJ/mol)	Ref.
DNL-9(Fe)	1136	1.281	5.45	2.48	28.0	This work
SIFSIX-3-Ni	223$^\dashv$	1.610	5.27	0.13$^\neq$	36.7	[25]
TIFSIX-2-Cu-i	685	1.269	5.18	6.5$^\neq$	46.3	[25]
SIFSIX-Cu-TPA	1330	0.995	8.26	5.3	39.1	[26]
SIFSIX-1(Cu)	1178	0.864	8.48	1.74	37	[27]
UTSA-200	612$^\times$	1.365	3.66	1.43	40	[28]
NCU-100a	358$^\lozenge$	1.535	4.55	-	60.5	[29]
UTSA-300-Zn	311$^\lozenge$	1.536	3.08	19	57.6	[30]
ZJU-74a	694	1.353	3.84	1.53	65.0	[31]
NTU-65	680	1.106	3.35	-	-	[32]
ZJUT-2a*	350$^\times$	1.890	3.39	10*	41.5	[33]
BSF-3	458	0.950	2.77	8	42.7	[34]
BSF-1	535	1.046	2.37	2.4	30.7	[35]
ZJU-280a	810	1.008‡	4.73	18.1	50.6	[36]
DICRO-4-Ni-i	398	1.215	1.92	13.9	37.7	[37]
JCM-1	550	1.331	3.35	13.2	36.9	[38]
BSF-4	437	1.116	2.37	9.8	35	[39]
ZNU-1	532	1.118	3.39	56.6‡	54	[40]
GeFSIX-14-Cu-I (ZU-33)	424	1.333	3.97	-	56.6	[41]
SDU-CP-1	1987	0.764	3.79	2.5$^\neq$	27.9	[42]
GeFSIX-dps-Cu	310$^\lozenge$	1.606	4.04	171.9	58.5	[43]
[Zn₄F₄]-1a	568	1.135	3.55	4.12	28.2	[44]
NTU-61	2322	0.732	7.77	5	28.2	[45]
ZNU-4	258	-	3.79	9	50.3	[46]

$^\square$ The theoretical density in crystallography.

$^{\dashv,\times,\lozenge}$ Surface area were calculated from the CO_2 sorption data at 273, 196 or 195 K.

† Q_{st} is the value for the isosteric heat of adsorption at zero coverage.

* 296 K. ‡293 K.

$^\neq$ C_2H_2/CO_2 ratio is 2:1.

Table S11. Summary of the C_2H_2 static capacity, C_2H_2/CO_2 breakthrough time and normalized C_2H_2 breakthrough capacity at 298 K of the reported MOF adsorbents

Adsorbents	C_2H_2 capacity at 298 K (ml/g)	C_2H_2/CO_2 breakthrough time at 298 K (min/g)	Normalized C_2H_2 breakthrough capacity at 298 K (ml/g)	Ref.
DNL-9(Fe)	122	26 [a]	50	This work
CAU-10-H ≠	89.8	40 [b]	40	[47]
MIL-160(Al)	208	108 [b]	108	[48]
JNU-1	65	60 [b]	60	[49]
FJU-H8-Me	229	90 [b]	90	[50]
UiO-66-tetrazol	94	82 [b]	82	[51]
ZJUT-2a	76	15 [b]	15	[33]
UTSA-300a	70	12 [b]	12	[30]
TCuBr	63	100 [c]	50	[52]
ZJU-74a ≠	86	36 [b]	36	[31]
CPL-1-NH2	41	28 [b]	28	[53]
TCuCl	67	80 [c]	40	[52]
NTU-54 *	30	12 [c]	6	[54]
[Ni2(BTEC)(bipy)3]	77	32 [d]	19	[55]
FeNi-M'MOF	96	16 [b]	16	[56]
[Cu(BDCBr)(H2O)0.5 (DMF)2.5]	34	5 [b]	5	[57]
FJU-99	85	29 [e]	9	[58]
JXNU-5	56	10 [b]	10	[59]
NTU-53 *	63	13 [c]	6.5	[54]
SNNU-45	134	79 [b]	79	[60]
ZJU-196a	84	7.5 [b]	7.5	[61]
TIFSIX-2-Cu-i	92	100 [f]	100	[25]
ZJNU-13	118	58 [b]	58	[62]
FJU-90a	180	22 [b]	22	[63]
FJU-6-TATB	110	34 [g]	5.1	[64]
UTSA-74a	108	20 [b]	20	[65]
SNNU-63	91	30 [b]	30	[66]
SNNU-27-Fe	182	88 [b]	88	[67]
ZJU-280a ≠	106	75 [b]	75	[36]
SIFSIX-Cu-TPA	185	114 [b]	114	[26]
NbU-10 ‡	62.5	15	f not mentioned	[68]
Cu-CPAH	131.8	235 [h]	58	[69]
ZNU-1	76.3	29.2 [d]	18	[40]

Normalized C_2H_2 breakthrough capacity (q; ml/g):

$$q = \frac{ft}{m}$$

Where t is the breakthrough window (or the separation time; min); f is the C_2H_2 flow rate

(ml/min) and m is the adsorbent weight (g).

f: ^{a} 5 ml/min; ^{b} 2 ml/min; ^{c} 1 ml/min; ^{d} 1.2 ml/min; ^{e} 6.2 ml/min (5:5:90 C_2H_2/CO_2/He); ^{f} 10 ml/min (10:5:85 C_2H_2/CO_2/He); ^{g} 3 ml/min (5:5:90 C_2H_2/CO_2/He); ^{h} 0.5 ml/min.

‡ 293 K; ≠ 296 K; * 273 K

Section 6 Reference

1. Y. Wang, J. Jiang, L. Hua, K. Hou, Y. Xie, P. Chen, W. Liu, Q. Li, S. Wang and H. Li, *Anal. Chem.*, 2016, **88**, 9047-9055.

2. Q. Wu, L. Hua, K. Hou, H. Cui, W. Chen, P. Chen, W. Wang, J. Li and H. Li, *Anal. Chem.*, 2011, **83**, 8992-8998.

3. G. M. Sheldrick, *Acta Crystallogr A*, 2008, **64**, 112-122.

4. O. V. Dolomanov, L. J. Bourhis, R. J. Gildea, J. A. K. Howard and H. Puschmann, *J. Appl. Crystallogr.*, 2009, **42**, 339-341.

5. A. L. Spek, *J. Appl. Crystallogr.*, 2003, **36**, 7-13.

6. A. L. Spek, *Acta Crystallogr. D Biol. Crystallogr.*, 2009, **65**, 148-155.

7. A. L. Spek, *Inorg. Chim. Acta*, 2018, **470**, 232-237.

8. A. L. Spek, *Acta Crystallogr E Crystallogr. Commun.*, 2020, **76**, 1-11.

9. D. A. Gomez-Gualdron, P. Z. Moghadam, J. T. Hupp, O. K. Farha and R. Q. Snurr, *J. Am. Chem. Soc.*, 2016, **138**, 215-224.

10. A. Galarneau, F. Villemot, J. Rodriguez, F. Fajula and B. Coasne, *Langmuir*, 2014, **30**, 13266-13274.

11. Y.-M. Gu, H.-F. Qi, S. Qadir, X.-W. Liu, T.-J. Sun, S.-S. Zhao, Z. Lai and S.-D. Wang, *ACS Sustain. Chem. Eng.*, 2021, **9**, 17310-17318.

12. M. E. Rivera-Ramos and A. J. Hernández-Maldonado, *Ind. Eng. Chem. Res.*, 2007, **46**, 4991-5002.

13. Y. A. B. Çengel, Michael A. , *Thermodynamics – An Engineering Approach.*, McGraw-Hill, Boston, MA., 1998.

14. L. Y. Li, L. F. Yang, J. W. Wang, Z. G. Zhang, Q. W. Yang, Y. W. Yang, Q. L. Ren and Z. B. Bao, *AIChE J.*, 2018, **64**, 3681-3689.

15. D. Peralta, G. Chaplais, A. Simon-Masseron, K. Barthelet, C. Chizallet, A. A. Quoineaud and G. D. Pirngruber, *J. Am. Chem. Soc.*, 2012, **134**, 8115-8126.

16. J. K. D. M. R. D. N. Theodorou., *Diffusion in Nanoporous Materials*, Wiley-VCH Verlag GmbH & Co. KGaA, 2012.

17. C. J., *The Mathematics of Diffusion*, Oxford university press, 1979.

18. G. Kresse and J. Furthmuller, *Compu. Mater. Sci.*, 1996, **6**, 15-50.

19. J. P. Perdew, K. Burke and M. Ernzerhof, *Phys. Rev. Lett.*, 1996, **77**, 3865-3868.

20. G. Kresse and D. Joubert, *Phys. Rev. B*, 1999, **59**, 1758-1775.

21. P. E. Blochl, *Phys. Rev. B Condens Matter*, 1994, **50**, 17953-17979.

22. V. A. Rassolov, M. A. Ratner, J. A. Pople, P. C. Redfern and L. A. Curtiss, *J. Comput. Chem.*, 2001, **22**, 976-984.

23. *Journal*, 2004.

24. A. D. Becke, *J. Chem. Phys.*, 1993, **98**, 5648-5652.

25. K. J. Chen, H. S. Scott, D. G. Madden, T. Pham, A. Kumar, A. Bajpai, M. Lusi, K. A. Forrest, B. Space, J. J. Perry and M. J. Zaworotko, *Chem*, 2016, **1**, 753-765.

26. H. Li, C. Liu, C. Chen, Z. Di, D. Yuan, J. Pang, W. Wei, M. Wu and M. Hong, *Angew. Chem. Int. Ed.*, 2021, **60**, 7547-7552.

27. X. Cui, K. Chen, H. Xing, Q. Yang, R. Krishna, Z. Bao, H. Wu, W. Zhou, X. Dong, Y. Han, B. Li, Q. Ren, M. J. Zaworotko and B. Chen, *Science*, 2016, **353**, 141-144.

28.   B. Li, X. Cui, D. O'Nolan, H. M. Wen, M. Jiang, R. Krishna, H. Wu, R. B. Lin, Y. S. Chen, D. Yuan, H. Xing, W. Zhou, Q. Ren, G. Qian, M. J. Zaworotko and B. Chen, *Adv. Mater.*, 2017, **29**.

29.   J. Wang, Y. Zhang, P. Zhang, J. Hu, R. B. Lin, Q. Deng, Z. Zeng, H. Xing, S. Deng and B. Chen, *J. Am. Chem. Soc.*, 2020, **142**, 9744-9751.

30.   R. B. Lin, L. Li, H. Wu, H. Arman, B. Li, R. G. Lin, W. Zhou and B. Chen, *J. Am. Chem. Soc.*, 2017, **139**, 8022-8028.

31.   J. Pei, K. Shao, J. X. Wang, H. M. Wen, Y. Yang, Y. Cui, R. Krishna, B. Li and G. Qian, *Adv. Mater.*, 2020, **32**, e1908275.

32.   Q. Dong, X. Zhang, S. Liu, R. B. Lin, Y. Guo, Y. Ma, A. Yonezu, R. Krishna, G. Liu, J. Duan, R. Matsuda, W. Jin and B. Chen, *Angew. Chem. Int. Ed.*, 2020, **59**, 22756-22762.

33.   H. M. Wen, C. Liao, L. Li, L. Yang, J. Wang, L. Huang, B. Li, B. Chen and J. Hu, *Chem. Commun. (Camb.)*, 2019, **55**, 11354-11357.

34.   Y. Zhang, J. Hu, R. Krishna, L. Wang, L. Yang, X. Cui, S. Duttwyler and H. Xing, *Angew. Chem. Int. Ed.*, 2020, **59**, 17664-17669.

35.   Y. Zhang, L. Yang, L. Wang, S. Duttwyler and H. Xing, *Angew. Chem. Int. Ed.*, 2019, **58**, 8145-8150.

36.   Q. L. Qian, X. W. Gu, J. Y. Pei, H. M. Wen, H. Wu, W. Zhou, B. Li and G. D. Qian, *J. Mater. Chem. A*, 2021, **9**, 9248-9255.

37.   H. S. Scott, M. Shivanna, A. Bajpai, D. G. Madden, K. J. Chen, T. Pham, K. A. Forrest, A. Hogan, B. Space, J. J. Perry Iv and M. J. Zaworotko, *ACS Appl. Mater. Interfaces*, 2017, **9**, 33395-33400.

38.   J. Lee, C. Y. Chuah, J. Kim, Y. Kim, N. Ko, Y. Seo, K. Kim, T. H. Bae and E. Lee, *Angew. Chem. Int. Ed.*, 2018, **57**, 7869-7873.

39.   Y. Zhang, L. Wang, J. Hu, S. Duttwyler, X. Cui and H. Xing, *CrystEngComm*, 2020, **22**, 2649-2655.

40.   L. Wang, W. Sun, Y. Zhang, N. Xu, R. Krishna, J. Hu, Y. Jiang, Y. He and H. Xing, *Angew. Chem. Int. Ed.*, 2021, **60**, 22865-22870.

41.   Z. Zhang, X. Cui, L. Yang, J. Cui, Z. Bao, Q. Yang and H. Xing, *Indu. Eng. Chem. Res.*, 2018, **57**, 7266-7274.

42.   T. Li, P. Cui and D. Sun, *Inorg. Chem.*, 2022, **61**, 4251-4256.

43.   J. Wang, Y. Zhang, Y. Su, X. Liu, P. Zhang, R. B. Lin, S. Chen, Q. Deng, Z. Zeng, S. Deng and B. Chen, *Nat. Commun.*, 2022, **13**, 200.

44.   W. J. Shi, Y. Z. Li, J. Chen, R. H. Su, L. Hou, Y. Y. Wang and Z. Zhu, *Chem. Commun. (Camb.)*, 2021, **57**, 12788-12791.

45.   H. Wang, Y. Duan, Y. Wang, Y. Huang, K. Ge, S. Wang, B. Zheng, Z. Wang, J. Bai and J. Duan, *ACS Appl. Mater. Interfaces*, 2022, **14**, 13550-13559.

46.   N. Xu, J. B. Hu, L. Y. Wang, D. Luo, W. Q. Sun, Y. Q. Hu, D. M. Wang, X. L. Cui, H. B. Xing and Y. B. Zhang, *Chem. Eng. J.*, 2022, **450**, 138034.

47.   J. Pei, H. M. Wen, X. W. Gu, Q. L. Qian, Y. Yang, Y. Cui, B. Li, B. Chen and G. Qian, *Angew. Chem. Int. Ed.*, 2021, **60**, 25068-25074.

48.   Y.-M. Gu, H.-F. Qi, T.-T. Sun, X.-W. Liu, S. Qadir, T.-J. Sun, D.-F. Li, S.-S. Zhao, D. Fairen-Jimenez and S.-D. Wang, *Chem. Mater.*, 2022, **34**, 2708-2716.

49.   H. Zeng, M. Xie, Y. L. Huang, Y. Zhao, X. J. Xie, J. P. Bai, M. Y. Wan, R. Krishna, W. Lu and D. Li, *Angew. Chem. Int. Ed.*, 2019, **58**, 8515-8519.

50.   Z. Di, C. Liu, J. Pang, C. Chen, F. Hu, D. Yuan, M. Wu and M. Hong, *Angew. Chem. Int. Ed.*, 2021, **60**, 10828-10832.

51. W. Fan, S. B. Peh, Z. Zhang, H. Yuan, Z. Yang, Y. Wang, K. Chai, D. Sun and D. Zhao, *Angew. Chem. Int. Ed.*, 2021, **60**, 17338-17343.

52. S. Mukherjee, Y. He, D. Franz, S. Q. Wang, W. R. Xian, A. A. Bezrukov, B. Space, Z. Xu, J. He and M. J. Zaworotko, *Chemistry*, 2020, **26**, 4923-4929.

53. L. Yang, L. Yan, Y. Wang, Z. Liu, J. He, Q. Fu, D. Liu, X. Gu, P. Dai, L. Li and X. Zhao, *Angew. Chem. Int. Ed.*, 2021, **60**, 4570-4574.

54. S. Liu, Y. Huang, Q. Dong, H. Wang and J. Duan, *Inorg. Chem.*, 2020, **59**, 9569-9578.

55. Y. Du, Y. Chen, Y. Wang, C. He, J. Yang, L. Li and J. Li, *Sep. Purif. Technol.*, 2021, **256**.

56. J. Gao, X. Qian, R. B. Lin, R. Krishna, H. Wu, W. Zhou and B. Chen, *Angew. Chem. Int. Ed.*, 2020, **59**, 4396-4400.

57. H. Cui, Y. X. Ye, H. Arman, Z. Q. Li, A. Alsalme, R. B. Lin and B. L. Chen, *Cryst. Growth Des.*, 2019, **19**, 5829-5835.

58. T. Chen, Y. X. Ye, M. Yin, L. J. Chen, Z. J. Ke, J. Z. Guo, M. X. Zhang, Z. Z. Yao, Z. J. Zhang and S. C. Xiang, *Cryst. Growth Des.*, 2020, **20**, 2099-2105.

59. R. Liu, Q. Y. Liu, R. Krishna, W. Wang, C. T. He and Y. L. Wang, *Inorg. Chem.*, 2019, **58**, 5089-5095.

60. Y. P. Li, Y. Wang, Y. Y. Xue, H. P. Li, Q. G. Zhai, S. N. Li, Y. C. Jiang, M. C. Hu and X. Bu, *Angew. Chem. Int. Ed.*, 2019, **58**, 13590-13595.

61. L. Zhang, K. Jiang, L. Li, Y. P. Xia, T. L. Hu, Y. Yang, Y. Cui, B. Li, B. Chen and G. Qian, *Chem. Commun. (Camb.)*, 2018, **54**, 4846-4849.

62. T. T. Xu, Z. Z. Jiang, P. X. Liu, H. N. Chen, X. S. Lan, D. L. Chen, L. B. Li and Y. B. He, *ACS Appl. Nano Mater.*, 2020, **3**, 2911-2919.

63. Y. Ye, Z. Ma, R. B. Lin, R. Krishna, W. Zhou, Q. Lin, Z. Zhang, S. Xiang and B. Chen, *J. Am. Chem. Soc.*, 2019, **141**, 4130-4136.

64. L. Liu, Z. Yao, Y. Ye, Y. Yang, Q. Lin, Z. Zhang, M. O'Keeffe and S. Xiang, *J. Am. Chem. Soc.*, 2020, **142**, 9258-9266.

65. F. Luo, C. Yan, L. Dang, R. Krishna, W. Zhou, H. Wu, X. Dong, Y. Han, T. L. Hu, M. O'Keeffe, L. Wang, M. Luo, R. B. Lin and B. Chen, *J. Am. Chem. Soc.*, 2016, **138**, 5678-5684.

66. Y. T. Li, J. W. Zhang, H. J. Lv, M. C. Hu, S. N. Li, Y. C. Jiang and Q. G. Zhai, *Inorg. Chem.*, 2020, **59**, 10368-10373.

67. Y. Y. Xue, X. Y. Bai, J. Zhang, Y. Wang, S. N. Li, Y. C. Jiang, M. C. Hu and Q. G. Zhai, *Angew. Chem. Int. Ed.*, 2021, **60**, 10122-10128.

68. J. Zhao, Q. Li, X. C. Zhu, J. Li and D. Wu, *Inorg. Chem.*, 2020, **59**, 14424-14431.

69. L. Meng, L. Yang, C. Chen, X. Dong, S. Ren, G. Li, Y. Li, Y. Han, Z. Shi and S. Feng, *ACS Appl. Mater. Interfaces*, 2020, **12**, 5999-6006.